International Journal of Electrical and Computer Engineering (IJECE)
Vol. 12, No. 5, October 2022, pp. 4841~4851
ISSN: 2088-8708, DOI: 10.11591/ijece.v12i5.pp4841-4851

Hybrid winding function method for inductance analysis of a line start synchronous reluctance machine

Redjem Rebbah, Mohamed Yazid Kaikaa, Loubna Boudjelida
Electrical Engineering Laboratory of Constantine, Department of Electrical Engineering, Sciences of Technology Faculty, Frères Mentouri Constantine 1 University, Algeria

Article Info

Article history:

Received Jul 28, 2021
Revised May 25, 2022
Accepted Jun 9, 2022

Keywords:

Conformal mapping
Finite element analysis
Hybrid winding function
Inductance profile
Line-start synchronous motor

ABSTRACT

In recent years, there has been renewed interest in line-start synchronous reluctance machines (LSSRMs) due to their simple construction, magnet-free rotor, and low cost. To improve control performance, design optimization, and fault diagnostic analysis of these machines, it requires accurate estimation of their electromagnetic characteristics using detailed and time-consuming finite element analyses (FEAs). In this paper, inductances and electromagnetic torque of the LSSRM were calculated using the combination of winding function analysis and conformal mapping instead of FEA. The hybrid approach can be applied to the prediction of motor behavior, taking into account all space harmonics of the air-gap permeance without any restriction on the rotor saliencies and topologies. The influence of the core saturation, stator slots, and rotor bars were also considered. The results obtained by simulations were compared with FEA in terms of accuracy and computational time.

This is an open access article under the CC BY-SA license.

Corresponding Author:

Redjem Rebbah
Electrical Engineering Laboratory of Constantine, Department of Electrical Engineering, Frères Mentouri Constantine 1 University
Constantine 25000, Algeria
Email: redjem.rebbah@umc.edu.dz

1. INTRODUCTION

Over the past decade, there has been sustained research activity on the line start synchronous reluctance machines [1]. Several studies have shown that these types of machines and their online starting ability are suitable for a wide variety of applications and are particularly attractive for variable-speed applications such as industrial conveyors [2], [3]. The line-start synchronous reluctance machine (LSSRM) starts as an asynchronous machine based on the induction-motor principle. Then, the machine is able to operate as a synchronous motor, reaching synchronous speed thanks to the reluctance torque [4]. In order to analyze this type of machine, several analytical and numerical approaches have been developed [5]. However, due to the special topology of the rotor, which combines saliency and rotor cage slots under magnetic saturation conditions, most of the proposed analytical approaches are rarely able to offer fast and accurate analyses of self-and mutual inductance characteristics [6]. The LSSRM electromagnetic torque splits into two components: a reluctance pulsating component and a constant component which is obtained when the machine is fed by a sinusoidal current [6]. Electromagnetic torque and machine armature winding inductances are both functions of rotor position and phase current. The torque and winding inductances can both be well determined by two well-known methods, numerically with finite element analysis or analytically with the classical winding function theory [6], [7]. An accurate result can still be obtained using finite element analysis (FEA). However, this approach is often difficult to apply and leads to significant

computational time [8]. The second method performs the integral over the mechanical position of the ratio of stator winding turns distribution to the air-gap permeance waveform [9], [10]. This method is highly effective because of its simplicity, but has insufficient accuracy due to the air-gap permeance of Fourier's function. This function, which is the sum of superimposed sine and cosine waves of changing amplitude, frequency, and phase, represents the decomposition of the air-gap permeance variation caused by the rotor saliency combined with the stator and rotor slot effects. The saturation influence was estimated using an equivalent air-gap length. Under transient conditions, each part of the motor core experiences different magnetic flux densities and different flux path lengths. Based on the equivalent air-gap length technique, the substituted air-gap length was computed and adjusted to the saturated conditions of the machine, which implied its enlargement. The LSSRM was described almost completely in terms of the geometrical characteristics of its air-gap, such as the air-gap length, slot opening width, and the number of slots. Once the air-gap geometry was defined, the execution of the proposed hybrid winding function theory (HWFT) developed by [11] was used to complete the self and mutual inductance calculation process. At several points, the approach does not require any dealing with complex physics principles involved in the whole LSSRM device structure. The technique closely follows the performance of the traditional FEA in terms of accuracy and computational time. In this work, two methods were used and compared for inductances and electromagnetic torque calculation, FEA and the new HWFT method using conformal mapping for the complex transformation of the air-gap permeance function. The obtained rotor permeance function was directly used in the analytical expression to compute self and mutual inductances. Both HWFT and FEA were compared in terms of accuracy and time-consuming process.

2. MATERIAL AND METHOD

2.1. Description of the LSSRM model

The rotor geometry of the LSSRM is similar to the rotor of an induction motor with a squirrel cage. The shape of the rotor is modified to a salient rotor by cropping four parts from the cylinder periphery core, which represents the four-rotor poles. The cropped areas around the rotor periphery were limited to one-fourth of the rotor radius to ensure a low ratio between d-axis and q-axis rotor inductance. Figure 1 shows the cross-section of the LSSRM with the standard three-AC stator structure with 40 slots. Table 1 shows the detailed machine dimensions. The study takes into account the saturation effect.

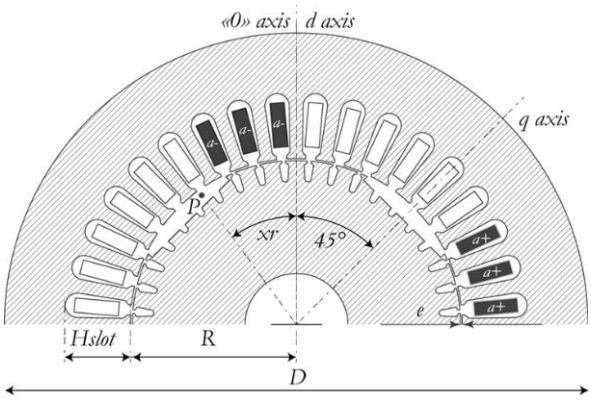

Figure 1. Line-start synchronous reluctance motor cross section

Table 1. Dimensions of the machine

Quantity and Symbol	Value
Stator outer diameter (D)	160 mm
Inner radius of the stator (R)	45.5 mm
Outer radius of the rotor (r)	45 mm
Constant air-gap length (e)	0.5 mm
Active axial length (L)	70 mm
Pole arc/pole pitch (β)	0.5
Number of poles pairs (P)	2 (4 poles)
Number of slots in the stator (n)	36
Turns per slot (N)	115
Stator slot pitch (τ)	10 degrees

2.2. Hybrid winding function theory and conformal mapping

The classical winding function theory was of great help for the analysis of standard electric machines, such as induction motors and DC motors. This method is still useful for transient and steady-state analyses of salient machine structures such as salient pole generators, switched reluctance motors, and permanent magnet synchronous generators [12]–[16]. The winding function expression consists of a definite integral involving the geometrical position of the phase winding which represents the magnetomotive force distribution across the air-gap obtained by (1) and the air-gap permeance profile that includes slotting and saliency effects [17], [18]. The geometrical position of the phase winding N_k can be expressed by the Fourier expansion as (1):

$$N_k(\emptyset) = \sum_{h=1}^{\infty} A(2h-1)cos\left((2h-1)\left(\phi - \frac{2(k-1)\pi}{2}\right)\right) \quad (1)$$

where A represents the numerical Fourier expansion of the total winding factor, which is equal here to the product of the distribution factor, the skewing, and the pitch factor [19]. The symbol k represents the stator phase a, b, or c. The waveform of N_k obtained by (1) for the phase a, b and c respectively is shown in Figure 2.

However, the classical winding function theory analysis gives only accurate results for machines with small smoothed air gap topologies. The rotor permeance equivalent function using the Fourier series often does not provide an accurate model for slotted structures [20], [21].

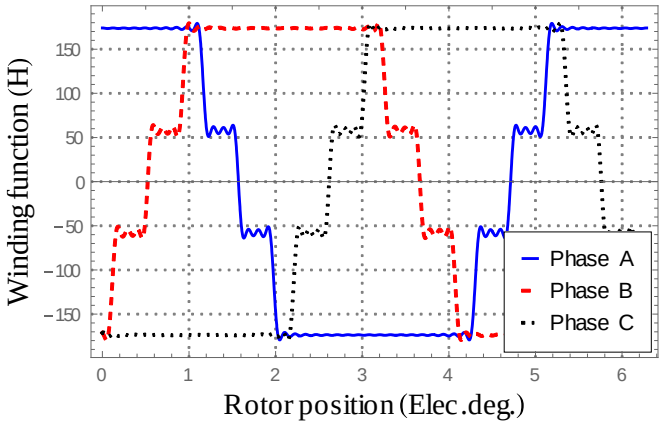

Figure 2. Winding function of the stator phases a, b and c

2.3. Rotor permeance function using conformal mapping

The technique proposed by [11]–[13], reviewed the air-gap permeance function using the MATLAB Schwartz-Christoffel (SC) Toolbox for conformal mapping transformation [14], [22]. The authors propose a numerical identification of the conformal map using the complex transformation technique instead of an explicit Fourier expansion for an accurate profile of the permeance. This was performed using a logarithmic complex function depicted in (2), which converts the polar coordinate of the circular real air-gap geometry named the S-plane into a complex plane in the Z-plane.

$$Z = log(S) \quad (2)$$

Figure 3 shows the air-gap geometry in Figure 3(a) and its permeance identification after SC mapping transformation in Figure 3(b). The numerical SC Toolbox [23] was used to obtain an open complex configuration of the planar polygon geometry which represent the map of the combined stator slots and rotor saliency with cage slots.

$$Z = A\int_{w_0}^{w} \prod_{k=1}^{n-1}(w' - w_k)^{\frac{\alpha_k}{\pi}-1} dw' + cst \quad (3)$$

Where A and cst are the equation constants relative to the integration, n is the number of vertices in the z-plane, $W_1, \dots, W_n$ are the points located in the canonical rectangle in the w-plane corresponding to the vertices and α_k are the angles of the polygon.

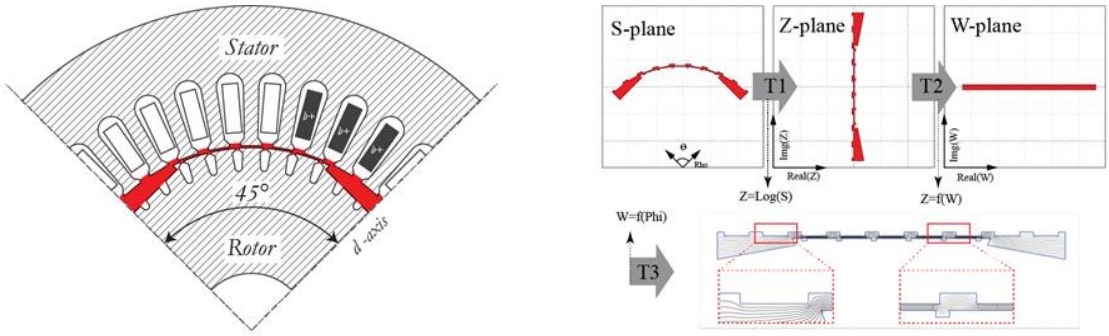

Figure 3. The inverse air-gap permeance mapping (a) physical air-gap and (b) flow chart of the inverse air-gap permeance identification of LSSRM by the usage of SC mapping

Using expression 3, the transformation leads to a canonical smooth rectangle called the w-plane of the stator geometry configuration, keeping the air-gap permeance easy to determine. The canonical rectangle represented in the w-plane provides the corresponding inverse gap waveform as shown in Figure 4.

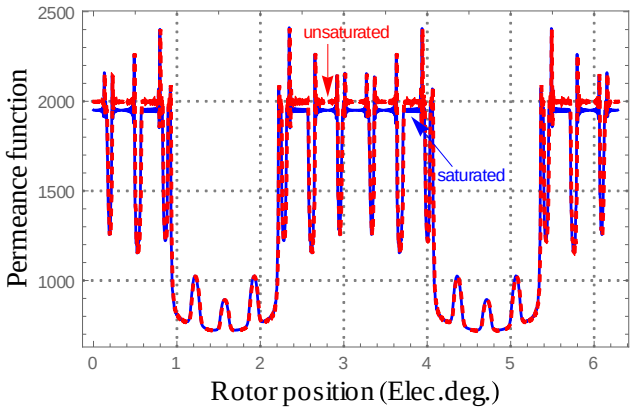

Figure 4. Saturated and unsaturated inverse air-gap waveform

The curve shows the permeance waveform for the unsaturated core material in a dashed line versus the saturated core material's. Once the permeance function P_{sr} is identified by the SC toolbox, the numerical Fourier expansion of the inverse gap waveform is calculated and presented by (4).

$$P_{sr}(x_r) = \sum_{h=1}^{\infty} P_h cos(h * x_r) \tag{4}$$

In order to calculate the flux density distribution along the air-gap circumference, which is produced by the stator AC rotating field, the winding function $N_a(\emptyset)$is multiplied by the inverse air-gap P_{sr} function and the phase current flowing in that winding [24].

$$B_a(x_r) = \mu_0 P_{sr}(\emptyset - x_r) N_a(\emptyset) i_a \tag{5}$$

Where i_a is the RMS current flowing in stator phase (A), N_a The number of coil turns. The magnetic flux between two stator phases k and k' can be expressed as (6).

$$\lambda_{kk'}(x_r) = i_a * L_{kk'}^{(ag)}(x_r) \tag{6}$$

$L_{kk'}(x_r)$ is the expression of two stator phases k, k' mutual inductance written as (7):

$$L_{kk'}(x_r) = l_{kk'}^{Leak} + L_{kk'}^{(ag)}(x_r) \tag{7}$$

where $l_{kk'}^{Leak}$ which is independent from the rotor position [25] represents the term accounting for magnetic flux leakage with analytical validation in [26] and the term $L_{k,k'}^{(ag)}$ is the magnetizing flux between two stator phases. The term $l_{i,j}^{(ag)}$ can be expressed using:

$$L_{kk'}(x_r) = RL\mu_0 \int_0^{2\pi} P_{sr}(\phi - x_r)\, N_k(\phi) * N_{k'}(\phi) d\phi \tag{8}$$

Fourier expansion of (1) and (5) can be substituted into 6 giving:

$$L_{kk'}(x_r) = RL\mu_0 \int_0^{2\pi} \sum_{m=1}^{\infty} A(2m-1) cos\left((2m-1)\left(\phi - \tfrac{2}{3}\pi(k-1)\right)\right) \sum_{n=1}^{\infty} A(2n-1)\, cos\left((2n-1)\left(\phi - \tfrac{2}{3}\pi(k'-1)\right)\right) * \sum_{h=1}^{\infty} P_h cos\big(h(\phi - x_r)\big)\, d\phi \tag{9}$$

Which can be written as:

$$L_{kk'}(x_r) = RL\mu_0 \sum_{h=1}^{\infty}\sum_{m=1}^{\infty}\sum_{n=1}^{\infty} Ph * A(2m-1) * A(2n-1) \int_0^{2\pi} cos(\, h(\varphi - xr)) * cos(\,(2m-1)(\varphi - \frac{2(k-1)\pi}{3})) * cos(\,(2n-1)(\varphi - \tfrac{2(k'-1)\pi}{3}))d\varphi \tag{10}$$

where, μ_0 is the air-gap permeability, i_a the current of the phase (A), x_r and ϕ, are the angular position of the rotor respect to the location of the stator reference axes and the position along the inner stator region respectively. The rotor outer radius of the LSSRM is a function of the angular position x_r, and the inverse air-gap length, presented by the expression 2 is also a function of the rotor position x_r [27].

In other words, the salient air-gap permeance varies and alternates periodically as the rotor rotates. As a result, two specific paths of the stator magnetic flux are identified. The first one is aligned with the direct rotor axis representing the pole's face region, which is standardly related to the small air-gap, and the second one is aligned with the rotor quadrature-axis position, which is related to the large air gap. Figure 5 shows the two-flux density; one is a high permeability path, the flux lines follow rotor iron paths crossing the minimum air-gap length, the second represents the maximum air-gap length with a low permeability path.

The direct and quadrature calculation of the magnetic flux density was done using one of these following calculation and curve arrangement: Shifting by an angle of 45° the spatial angle of the rotor permeance curve with the respect to the magnetomotive force in an electric degree. Or, shifting with the same angle the magnetomotive force of the three stator phases with the respect of the rotor permeance.

2.4. Stator tooth saturation modeling

The approach described in [11] was found to be an ideal framework for the calculation of the magnetic saturation of various parts of the core. The method can be easily adapted to tooth saturation analysis. Besides dividing the stator tooth only into a maximum of two regions, in our approach, the stator tooth body is represented by several polygons. Each polygon represents a region with different lengths and areas. The stator tooth is shown in Figure 6, where regions are delimited by different length polygon boundaries on the surface with crosshatch. By definition, the winding function theory (WFT) assumes the relative permeability of the LSSRM core is infinite. In this study, the saturation effect is taken into consideration using the technique proposed by [11].

The authors use the WFT method by means of infinite permeability assumptions, in which the saturation is substituted by adjusting the equivalent air-gap length. A suitable value for the length of the air gap has thus to be determined for all stator teeth. The saturation effect is simulated by increasing the air gap length between the stator teeth and the rotor periphery. The longer the air-gap, the more saturated the core. Saturation modeling includes the following steps: i) the virtual coil is wound so that it has a one-turn coil on each tooth; ii) the incremental self and mutual inductance were carried out depending on the rotor position; and iii) the current through each virtual coil must be determined. The tooth's MMF is equivalent to the current of it is corresponding tooth. At each rotor position the flux linkage for the corresponding virtual tooth coil are calculated.

The equivalent length *deltaLg* is the sum over the number of tooth sections ranged from 1 to the maximum section number n_{max} of the length body over the body sections times their respective permeability. here we choose only one section length due to the fact that the core permeability is not changing. The equivalent air-gap length *deltaLg* is presented by the following generalized (11):

$$deltaLg = \frac{At_{shoe}}{\mu_{rt_{shoe}}} + It_{shoe} * \sum_{n=1}^{n_{max}} \frac{It_{body}(n)}{At_{body}(n) * \mu t_{body}(n)} \tag{11}$$

where the parameters lt_{body} and lt_{shoe} represents the body and the shoe length, At_{body} and At_{shoe} represents the cross area for the body and the shoe respectively and μr_{tbody} and μrt_{shoe} for the relative permeability. Although the Schwartz-Christoffel Toolbox is a useful tool, it suffers from performance limitations due to the rotor slot opening.

The Schwartz-Christoffel MATLAB toolbox may not always be able to accurately calculate the equivalent polygon which contains the entire stator and rotor slotted geometry. For the studied model, the stator and rotor slotted geometry design was limited to only the slot opening region, which represents a third of the total slot height. The diagnostic algorithm process may lead to inaccuracies because of these incomplete slot geometries, which are not always considered effectively.

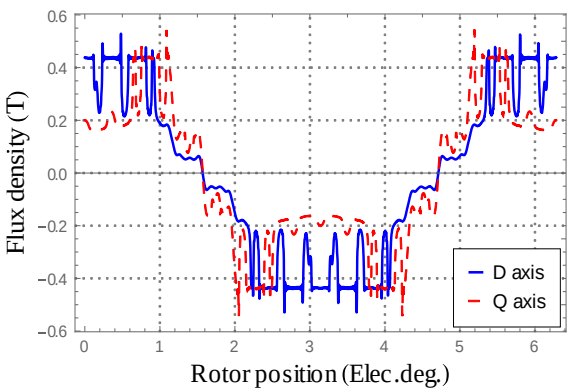

Figure 5. Air-gap flux density in d-axis and q-axis

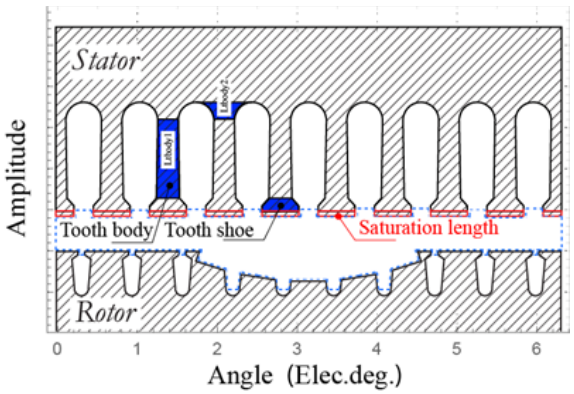

Figure 6. Stator tooth with virtual coil

3. RESULTS

The self and mutual inductances are calculated using expression 8 for various rotor positions; Figure 7 clearly shows ripples on the inductance profiles due to the slotting effects. the figure of the inductance waveforms shows the rotor saliency influence for various rotor positions that leads to an additional pulsating torque and supplements the average torque, when the rotor saliency ratio is high the torque profile will distort and may lead to a large a pulsating torque component.

3.1. Analytical calculation of the air-gap electromagnetic torque

The air-gap electromagnetic torque $T_{em}^{k}$of the kth armature phase, is calculated using the following derivative of the magnetic co-energy expression:

$$Tem^{(k)} = \left[\frac{\partial W_{co-energy}^{(k)}}{\partial x_r}\right]_{i=Cst} \tag{12}$$

The total torque is represented by the sum of the three armature phases contribution.

$$T_{airgap} = \sum_{k=a,b,c} T_{em}^{k} = \frac{1}{2}\begin{bmatrix} i_{as} & i_{bs} & i_{cs} \end{bmatrix} * \frac{\partial L(x_r)}{\partial x_r} * \begin{bmatrix} i_{as} \\ i_{bs} \\ i_{cs} \end{bmatrix} \tag{13}$$

Where T_{em}^{k} is the electromagnetic torque contribution of each armature phases and the total energy stored $W_{co-energy}$ represents the co-energy which is valid only for linear systems. i_{as}, i_{bs} and i_{cs} are the three-phase current supplying the stator winding. α is the angle that must be regulated to maximize the electromagnetic torque. here the control angle α was set to a value of 0.3245 rad.

$$\begin{cases} i_{as} = \sqrt{2i_m}\sin\left(xr - \frac{\alpha\pi}{3}\right) \\ i_{bs} = \sqrt{2i_m}\sin\left(x_r - \frac{1}{3}\left((4+\alpha)\pi\right)\right) \\ i_{cs} = \sqrt{2i_m}\sin\left(x_r - \frac{1}{3}\left((2+\alpha)\pi\right)\right) \end{cases} \tag{14}$$

$$L(x_r) = \begin{pmatrix} L_{saa} & L_{sab} & L_{sac} \\ L_{sba} & L_{sbb} & L_{sbc} \\ L_{sca} & L_{scb} & L_{scc} \end{pmatrix} \tag{15}$$

Where $L(x_r)$ represents the inductance matrix. this matrix allows the air-gap electromagnetic torque computation by means of (16). The current vector is shifted from the phase reference "a" with 45° electrical). The torque characteristics versus rotor position in electrical angle can be calculated as it is shown in Figure 8.

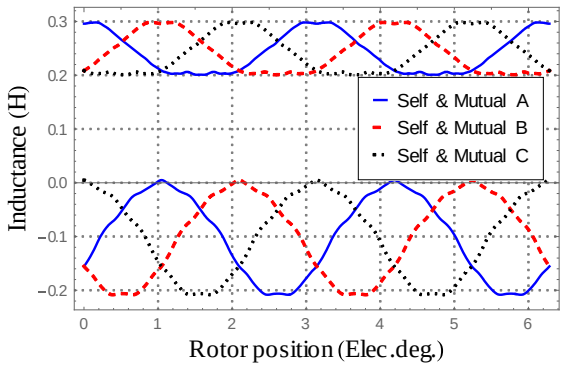

Figure 7. Winding function analysis with HWFT

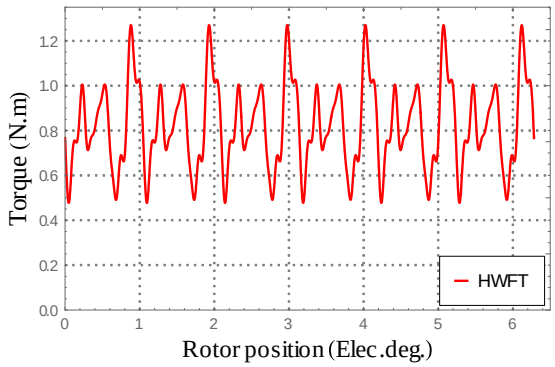

Figure 8. Calculated torque versus rotor position (δ=45°, I_{rms}=1 A); hybrid winding function method

3.2. Finite element analysis and hybrid winding function analysis comparison

3.2.1. The flux density distribution in the air-gap

Two-dimensional (2D) magnetostatic finite element analysis was carried out with the same set of parameters used for the winding function analysis. The 2D FEA was performed on the basis of a commercial software package [28]. Figure 9 (a)-(d) shows the radial air-gap flux density with respect to electrical degree on the d-axis in Figures 9(a) and 9(c) and q-axis in Figures 9(b) and 9(d) respectively. The flux density of the direct axis is slightly lower than the flux density of the quadrature axis, since the flux distribution in the d axis is denser than the quadratic axis flux distribution. The FEA results revealed good agreement with the HWFT results.

3.3. The finite element computation of stator inductances

In the stator stack, the phase winding self-inductance "a" can be calculated by using numerical integration techniques as well as the estimated value of the co-energy stored in the magnetic field that couples the adjacent phases. The inductance and the co-energy are expressed by (14) and (15):

$$L_{kk'} = \frac{2W_{kk}}{I^2} \tag{16}$$

$$W_{kk'} = \oint B_k H_{k'}, d\Omega \tag{17}$$

where, $W_{kk'}$ is the magnetic field energy located in the air-gap linking conductor k with conductor k', I_k represents the current in the "k" conductor, $B_k$is the magnetic flux density where the current flowing in the conductor k is equal to one ampere, $H_{k'}$ is the magnetic field where the current flowing in the conductor k' is also equal to one ampere. For multi-turn conductors, the inductance quantity is given by (16):

$$L_{net} = N^2 L_{matrix} \tag{18}$$

where L_{matrix} represents the matrix with self and mutual components for the three stator phases. The results obtained for self and mutual inductance profile by FEA (compared to those obtained with the HWFT) are shown in Figure 10. The self and mutual inductance harmonics are depicted respectively in Figure 11(a) and Figure 11(b). Both analysis of the finite element method and winding function theory expose similar results except for the direct component of the self-inductance [29]. The difference in the direct component is due to the leakage flux in the stator slots. The leakage flux is neglected while developing winding function calculations.

Computational time required for finite element analysis at a numerical resolution of π/100 rad takes around 11 minutes for a Xenon processor work station computer running Windows 7 with 12 GB RAM). The computational costs are in the range of 1 minute using the same PC with the winding function theory coded in the MATLAB programming language. Figure 12 shows the spectrum for the air-gap electromagnetic torque with respect to the amplitude over a frequency range of 0 to 40*f Hertz.

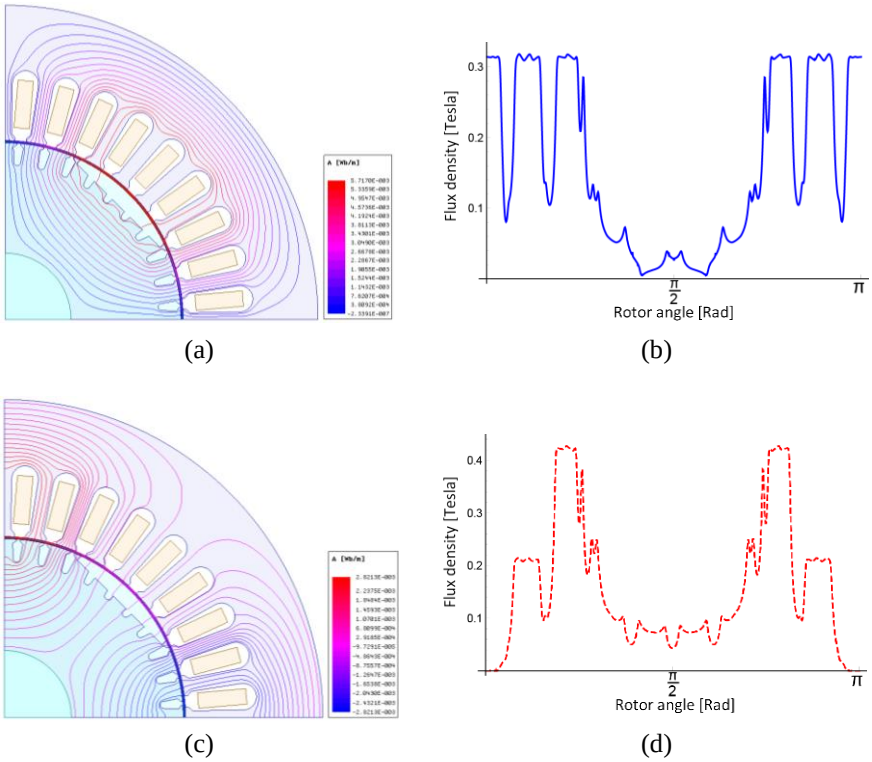

Figure 9. Comparing equipotential of (a), (b) the air-gap flux density with respect to electrical degree on the d-axis and (c), (d) equipotential in q-axis, respectively

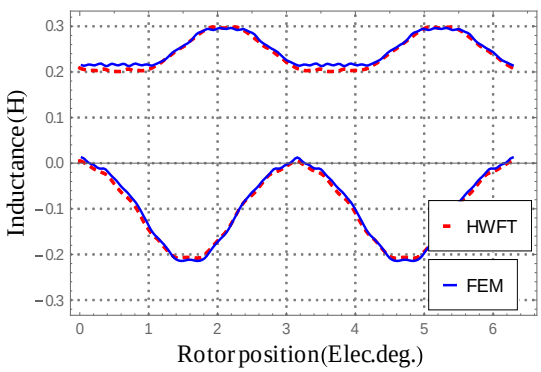

Figure 10. Winding function analysis vs FEM: self-inductance curve profile of the phase "a"; mutual inductance curve profile between a and b

3.4. The electromagnetic air-gap torque computation

The numerical approach uses the virtual work principle to compute the torque on the rotor region. Across the air-gap, the electromagnetic torque expression is given by the following relationship expressed by (17):

$$T_{air-gap} = \frac{\partial}{\partial \phi} \int_v \int_0^H B(\phi) dH(\phi) dv \tag{19}$$

where B represents the flux density and H is the air-gap flux intensity. Both B and H are a function of the angle φ. When computing electromagnetic torque, the mesh was mostly refined within the air-gap region, however, in order to save a lot of the computation time, the mesh operation performed with the dedicated software is adjusted to keep the mesh node number as low as possible during the iterations [30]. As expected from the inductance waveforms results, the torque profile shows a ripple caused by the stator and rotor slotting effect. The electromagnetic torque result illustrated in Figure 13 is in accordance with the result obtained with HWFT. The computational time required for finite element analysis takes around 660 seconds at a resolution of $\pi/100$ rad, the same processor computes the inductance profiles with the same resolution within 90 seconds.

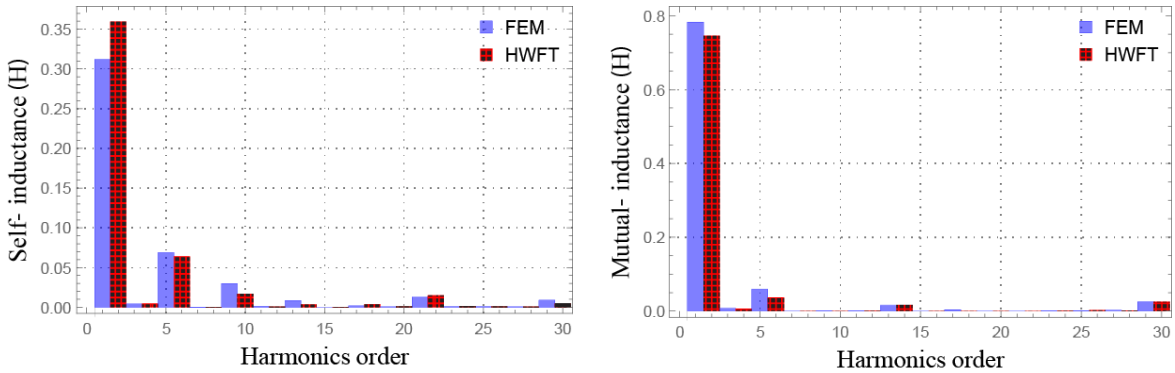

(a) (b)

Figure 11. Harmonic terms: (a) self-inductance, (b) mutual inductance for the two methods

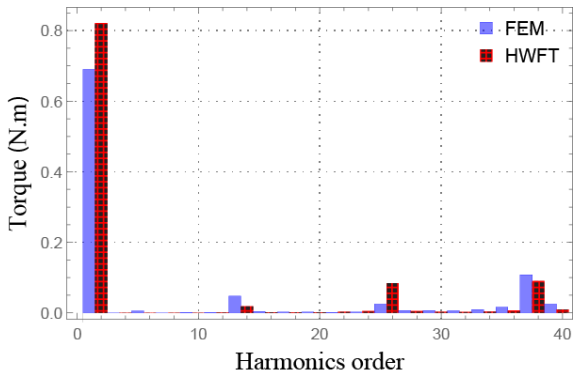

Figure 12. Harmonic terms of the electromagnetic torque for the two methods

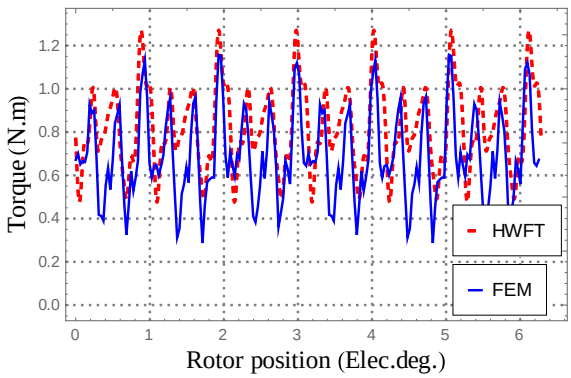

Figure 13. Winding function analysis vs FEA: electromagnetic torque versus rotor position (δ = 45°, I_{rms}=1 A); both HWFT and FEA

4. CONCLUSION

The main objective of this work is to investigate the hybrid winding function theory based on WFT and conformal mapping for improving performance and analysis of line start synchronous reluctance motors. The combination of the two techniques allows for accurate calculation of all space harmonics associated with the air-gap permeance without any restriction on the rotor saliencies, stator slots, and core saturation. The

results of calculations using hybrid winding function theory agree quite reasonably with the FEA results. This approach is well-suited for fast geometric parameter treatment when the LSSRM models are analyzed under saturated conditions. The hybrid winding function theory can also be used for design, optimization, and fault diagnosis in electric machines.

REFERENCES

[1] S. T. Boroujeni, M. Haghparast, and N. Bianchi, "Optimization of flux barriers of line-start synchronous reluctance motors for transient- and steady-state operation," *Electric Power Components and Systems*, vol. 43, no. 5, pp. 594–606, Mar. 2015, doi: 10.1080/15325008.2014.984819.

[2] A. Kersten, Y. Liu, D. Pehrman, and T. Thiringer, "Rotor design of line-start synchronous reluctance machine with round bars," *IEEE Transactions on Industry Applications*, vol. 55, no. 4, pp. 3685–3696, Jul. 2019, doi: 10.1109/TIA.2019.2914010.

[3] R. F. Schiferl and T. A. Lipo, "Power capability of salient pole permanent magnet synchronous motors in variable speed drive applications," *IEEE Transactions on Industry Applications*, vol. 26, no. 1, pp. 115–123, 1990, doi: 10.1109/28.52682.

[4] S.-H. Ha, J.-P. Hong, J.-Y. Lee, H. Nam, and G.-H. Kang, "Rotor design of line-start synchronous reluctance motor to improve starting performance," *WSEAS Transactions on Systems*, vol. 4, no. 9, pp. 1425–1431, 2005

[5] V. Abramenko, I. Petrov, and J. Pyrhonen, "Analysis of damper winding designs for direct-on-line synchronous reluctance motor," in *IECON 2017 - 43rd Annual Conference of the IEEE Industrial Electronics Society*, Oct. 2017, pp. 1802–1809, doi: 10.1109/IECON.2017.8216305.

[6] S. Guenther and W. Hofmann, "Multi-objective tradeoffs in the design optimization of synchronous reluctance machines for electric vehicle application," in *2015 IEEE International Electric Machines & Drives Conference (IEMDC)*, May 2015, pp. 1715–1721, doi: 10.1109/IEMDC.2015.7409295.

[7] T. Hamiti, T. Lubin, and A. Rezzoug, "A simple and rfficient tool for design Analysis of synchronous reluctance motor," *IEEE Transactions on Magnetics*, vol. 44, no. 12, pp. 4648–4652, Dec. 2008, doi: 10.1109/TMAG.2008.2004536.

[8] R. Chehda, N. Benouzza, A. Bendiabdellah, and N. K. Belghitri, "A combined variable reluctance network-finite element VR machine modeling for stator inter-turn short-circuit diagnosis," *International Journal of Electrical and Computer Engineering (IJECE)*, vol. 10, no. 1, pp. 105–116, Feb. 2020, doi: 10.11591/ijece.v10i1.pp105-116.

[9] T. Hamiti, T. Lubin, L. Baghli, and A. Rezzoug, "Modeling of a synchronous reluctance machine accounting for space harmonics in view of torque ripple minimization," *Mathematics and Computers in Simulation*, vol. 81, no. 2, pp. 354–366, Oct. 2010, doi: 10.1016/j.matcom.2010.07.024.

[10] E. S. Obe, "Calculation of inductances and torque of an axially laminated synchronous reluctance motor," *IET Electric Power Applications*, vol. 4, no. 9, pp. 783–792, 2010, doi: 10.1049/iet-epa.2009.0197.

[11] J. Faiz and F. Rezaee-Alam, "A new hybrid analytical model based on winding function theory for analysis of surface mounted permanent magnet motors," *COMPEL - The International Journal for Computation and Mathematics in Electrical and Electronic Engineering*, vol. 38, no. 2, pp. 745–758, Mar. 2019, doi: 10.1108/COMPEL-08-2018-0303.

[12] B. Asad, T. Vaimann, A. Kallaste, A. Rassolkin, and A. Belahcen, "Winding function based analytical model of squirrel cage induction motor for fault diagnostics," in *2019 26th International Workshop on Electric Drives: Improvement in Efficiency of Electric Drives (IWED)*, Jan. 2019, pp. 1–6, doi: 10.1109/IWED.2019.8664314.

[13] X. Tu, L.-A. Dessaint, M. El Kahel, and A. O. Barry, "A new model of synchronous machine internal faults based on winding distribution," *IEEE Transactions on Industrial Electronics*, vol. 53, no. 6, pp. 1818–1828, Dec. 2006, doi: 10.1109/TIE.2006.885125.

[14] S. S. Maroufian, "Winding function modeling of synchronous reluctance machines," Ph.D Thesis, Concordia University, 2018.

[15] L. Serrano-Iribarnegaray, P. Cruz-Romero, and A. Gomez-Exposito, "Critical review of the modified winding function theory," *Progress In Electromagnetics Research*, vol. 133, pp. 515–534, 2013, doi: 10.2528/PIER12091301.

[16] P. Naderi, "Torque/current spectral analysis for healthy and eccentricity faulty synchronous reluctance machine using mathematical modeling method," *International Transactions on Electrical Energy Systems*, vol. 26, no. 8, pp. 1625–1645, Aug. 2016, doi: 10.1002/etep.2165.

[17] J. Figueroa, J. Cros, and P. Viarouge, "Generalized transformations for polyphase phase-modulation motors," *IEEE Transactions on Energy Conversion*, vol. 21, no. 2, pp. 332–341, Jun. 2006, doi: 10.1109/TEC.2005.859965.

[18] J. Laksar and L. Veg, "Reduced schwarz-christoffel conformal mapping in surface-mounted PMSM," in *2018 18th International Conference on Mechatronics - Mechatronika (ME)*, 2019, pp. 1–9.

[19] Y. Chang, J. Jiao, G. Li, X. Liu, C. He, and B. Wu, "Effects of excitation system on the performance of magnetic-flux-leakage-type non-destructive testing," *Sensors and Actuators A: Physical*, vol. 268, pp. 201–212, Dec. 2017, doi: 10.1016/j.sna.2017.08.009.

[20] F. R. Alam and K. Abbaszadeh, "Magnetic field analysis in eccentric surface-mounted permanent-magnet motors using an improved conformal mapping method," *IEEE Transactions on Energy Conversion*, vol. 31, no. 1, pp. 333–344, Mar. 2016, doi: 10.1109/TEC.2015.2479562.

[21] B. Rezaeealam and F. Rezaee-Alam, "An improved conformal mapping method for magnetic field analysis in surface mounted permanent magnet motors," *COMPEL - The international journal for computation and mathematics in electrical and electronic engineering*, vol. 36, no. 4, pp. 892–905, Jul. 2017, doi: 10.1108/COMPEL-07-2016-0284.

[22] A. Ouammi, D. Zejli, H. Dagdougui, and R. Benchrifa, "Artificial neural network analysis of Moroccan solar potential," *Renewable and Sustainable Energy Reviews*, vol. 16, no. 7, pp. 4876–4889, Sep. 2012, doi: 10.1016/j.rser.2012.03.071.

[23] T. A. Driscoll and L. N. Trefethen, "Why use schwarz–christoffel maps?," in *Schwarz-Christoffel mapping*, Cambridge ; New York: Cambridge University Press, 2002.

[24] M. Cheng, P. Han, and W. Hua, "General airgap field modulation theory for electrical machines," *IEEE Transactions on Industrial Electronics*, vol. 64, no. 8, pp. 6063–6074, Aug. 2017, doi: 10.1109/TIE.2017.2682792.

[25] A. Tessarolo, *Modeling and analysis of multiphase electric machines for high-power applications*. Springer, 2011.

[26] A. Tessarolo, "Modeling and analysis of synchronous reluctance machines with circular flux barriers through conformal mapping," *IEEE Transactions on Magnetics*, vol. 51, no. 4, pp. 1–11, Apr. 2015, doi: 10.1109/TMAG.2014.2363434.

[27] T. A. Lipo, "Synchronous reluctance machines-A viable alternative for AC Drives?," *Electric Machines & Power Systems*, vol. 19, no. 6, pp. 659–671, Nov. 1991, doi: 10.1080/07313569108909556.

[28] CEDRAT, *User guide Flux® 11.2*, 2013. Accessed: Aug. 11, 2021 [Online]. Available:

http://www.tianyuantech.com/download/flux112.pdf
[29] T. Lubin, T. Hamiti, H. Razik, and A. Rezzoug, "Comparison between finite-element analysis and winding function theory for inductances and torque calculation of a synchronous reluctance machine," *IEEE Transactions on Magnetics*, vol. 43, no. 8, pp. 3406–3410, Aug. 2007, doi: 10.1109/TMAG.2007.900404.
[30] K. Boughrara, D. Zarko, R. Ibtiouen, O. Touhami, and A. Rezzoug, "Magnetic field analysis of inset and surface-mounted permanent-magnet synchronous motors using schwarz–christoffel transformation," *IEEE Transactions on Magnetics*, vol. 45, no. 8, pp. 3166–3178, Aug. 2009, doi: 10.1109/TMAG.2009.2016559.

BIOGRAPHIES OF AUTHORS

Redjem Rebbah received his M.S. and Ph.D. degrees from the Frères Mentouri Constantine 1 University. He is currently an Associate Professor and researcher in the Electrical Engineering Department of the Faculty of Technological Sciences at the University of Mentouri Constantine 1, Algeria. His current research interests are CAD and failure analysis of electrical machines and renewable energy conversion in micro-grids. He can be contacted at email: redjem.rebbah@umc.edu.dz.

Mohamed Yazid Kaikaa received his M.S. and Ph.D degrees in electrical engineering from the Electrical Department, Frères Mentouri, Constantine 1 University, Algeria, in 2002, 2005, and 2010 respectively. He is currently an assistant professor in in the Electrical Engineering Department of the Faculty of Technological Sciences at the University of Mentouri Constantine 1, Algeria. His fields of research include the modeling, the monitoring conditions of electrical machines and the power systems. He can be contacted at email: yazid.kaikaa@gmail.com.

Loubna Boudjelida received the bachelor degree in electrical engineering in 2013 and Master's degree in management and transformation of electrical energy in 2015 from Frères Mentouri Constantine 1 University, Algeria. She is currently a Ph.D. student at electrical engineering laboratory of Constantine, Algeria. The research area interests in design and optimization of electrical machines, diagnostics and control systems. She can be contacted at email: boudjelida_loubna@hotmail.com.